Optical and Quantum Electronics (2020) 52:88
https://doi.org/10.1007/s11082-020-2214-0

Thermal and dynamic effects of laser irradiation of thin metal films

V. V. Shepelev[1] · **N. A. Inogamov**[2] · **S. V. Fortova**[1]

Received: 28 October 2019 / Accepted: 16 January 2020

Abstract

The problem of irradiation of a thin gold film deposited on a glass substrate by a narrowly focused single femtosecond laser pulse is considered. Different surface structures can emerge depending on amount of radiation energy absorbed by an irradiated surface.The most important thermal driver for the formation of surface structures is the lateral electron heat flow in the film. This effect consists from three stages: (1) the distribution of the absorbed in the skin layer of laser energy from the frontal boundary of the film to the rear boundary to equalize the temperature; (2) lateral transfer of energy along the film from the center to the edges; (3) cooling and recrystallization of the heated region of the light spot. A model for the study of the effect is presented based on the two-temperature equations of S. I. Anisimov and coauthors and the semi-empirical wide-range equation of state of metal. The model takes into account Gaussian pulse absorption, electron thermal conductivity and electron-ion relaxation in the metal. If the invested energy is large enough, the shock-wave effect on the formation of holes in the film becomes possible. It includes following stages: (1) generation of a shock wave in the glass due to the transfer of energy from the metal; (2) spherization of the formed shock wave, i.e. transition from one-dimensional to two-dimensional propagation mode; (3) transverse propagation of the shock wave in the substrate along the boundary with the film; (4) accumulation of momentum of a film in direction of vacuum. Pressure behind the shock pushes material of a film away from the substrate. When material of a film accumulates enough momentum (and thus velocity in direction to vacuum) it loses connection with substrate. This leads to formation of a hole. Layers of backing material at the same time acting on film as the pistons. A hydrodynamic model for the study of holes formation based on the equations of hydrodynamics of the ideal Euler medium is presented.

Keywords Laser–matter interaction · Femtosecond laser ablation · Hydrodynamics · Equations of state

---

This article is part of the Topical Collection on Fundamentals of Laser Assisted Micro- and Nanotechnologies.

Guest edited by Tigran Vartanyan, Vadim Veiko, Andrey Belikov and Eugene Avrutin.

✉ V. V. Shepelev
vadim.aries@gmail.com

Extended author information available on the last page of the article

1 Introduction

An interest to ultrashort pulse lasers has not diminished due to a huge number of applications in nonlinear optics, spectroscopy, particle acceleration, directed beam generation, micro- and nanoelectronics, telecommunications, medicine and other areas of modern science and technology (Kryukov 2008). An important application of femtosecond laser ablation of materials is to obtain surface structures with different physical properties. The smooth surface of the substance after action of ultrashort laser pulse becomes nanostructured.

Speaking of laser-induced surface structures, the periodic surface structures of LIPSS (Bonse et al. 2017) discovered in the middle of the last century should be mentioned first. At higher intensities exceeding the thermomechanical ablation threshold, so-called random or chaotic surface structures arise (Vorobyev and Guo 2006; Fang et al. 2017). They are observed in the case of irradiation of thick targets and wide spots, compared, respectively, with the thickness of the heating zone and the size of the foaming zone. The intermediate position is occupied by structures that are observed when the energy threshold of thermomechanical ablation is not too much exceeded. As the energy invested increases, these can be explosions, jets, and holes (Wang et al. 2017; Nakata et al. 2003; Meshcheryakov and Bulgakova 2006; Meshcheryakov et al. 2013) arising in thin metal films sprayed onto glass substrates. We will consider the film thin, if its thickness does not exceed the heating zone of the metal, which is 50–150 nm for gold. Laboratory glass is often used as a substrate. In any case, the substrate must be thick enough to avoid destruction as a result of interaction with the shock wave caused by laser heating.

2 Thermal model

Sometimes films are fabricated of copper, nickel or multi-layer plastic for applications in electronics, but more often they are made of gold or silver. Consider the action of a single femtosecond laser pulse on a typical aluminium film of 50 nm, 1 nm = 10^{-9} m thick. The thickness of the skin layer is 15 nm for optical lasers, the pulse duration $\tau_L = 15$ fs, 1 fs = 10^{-15} s, the diameter of the light spot $2R_L = 360$ nm, $R_L = 180$ nm. Let's connect the longitudinal direction parallel to the laser beam with the x-axis. The perpendicular direction will be the y-axis. As a result of laser radiation, the film melts and later cools and recrystallizes. The two-temperature stage (2T-stage) is essential in this process, i.e. the model of the phenomenon must take into account the absorption of laser pulse energy by the electron subsystem, its subsequent transfer in the metal and relaxation between the electron and ion subsystems.

2.1 Overall description of processes

Absorption of a femtosecond laser pulse initiates the following processes:

1. Laser illumination of a focal spot with a diameter of $2R_L$ on the surface of the film.
2. Energy absorption and heating of the electronic subsystem in the skin layer within the focal spot. The distribution of energy during heating in the direction from the center

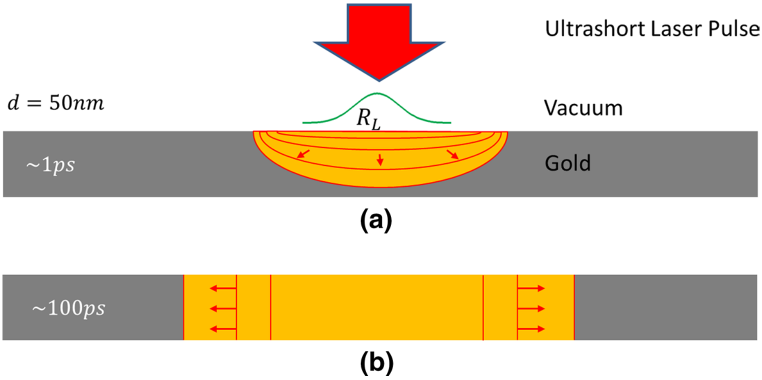

Fig. 1 The process of heat propagation after absorption of laser energy in a thin layer of metal is shown. **a** First, the heat propagates mainly along the normal to the surface, since the electron temperature gradient in this direction greatest. As a result, the electron temperature is aligned with the normal to the surface. **b** The absorbed energy then begins to flow laterally through the film. Heat flows from the film to the substrate are neglected because the thermal conductivity of the substrate is small

to the edges of the spot corresponds to the intensity distribution in the laser beam. See Fig. 1a.

3. Rapid redistribution of the energy of the electronic subsystem in the longitudinal direction, i.e. deep into the film. The term “ballistic transport” has previously been used to describe this process. The driver of the process is the electronic thermal conductivity. It becomes significant because of the strong heating of the electronic subsystem due to the absorbed pulse. The process takes place during about 1 ps, 1 ps = 10^{-12} s, until the approximate alignment of the electron temperature in the longitudinal direction, i.e. deep into the film. The speed of heating the film at this stage is several times higher than the speed of sound. The transverse distribution of electronic energy in the film during this time does not have time to change significantly because of the difference in spatial scales by an order of magnitude. Therefore, the energy distribution along the film boundary remains inhomogeneous. See Fig. 1a.
4. Slower alignment of the electron energy in the metal in the transverse direction. At this stage, the longitudinal component of the electron temperature gradient directed deep into the film is already small, and the transverse component of the electron temperature gradient becomes significant. The transverse component is significantly less than the maximum value in stage 2, so this stage lasts several times longer than stage 3. Referring to the two-dimensional approximation, here we can talk about the “turning” of the heat flow: in the previous stage, the main energy transfer went from the front wall of the film to the rear, and now split into two parts and turned 90°, from the center to the edges. Parallel to the electron thermal conductivity, electron-ion relaxation occurs at stages 2–3, which eventually leads to a practical coincidence of the profiles of the electron and ion temperatures. That is, with stage 3, the 2T-stage is also completed, and the process is then single-temperature. It can also be called a single-temperature stage (1T-stage), as opposed to a 2T-stage. See Fig. 1b.
5. And finally, due to cooling in the transverse direction, the melted gold temperature decreases within the light spot with a diameter of $2R_L$. Gradually the metal solidifies.

2.2 Model equations

Before creating a fully two-dimensional model, the authors used a one-dimensional hydrodynamic code for modeling (Inogamov et al. 2010, 2011). The lateral transfer of heat by electrons was further modeled using analytical estimates with either κ_e constant electron thermal conductivity or the insertion of a short two-temperature stage. In the two-dimensional thermal model, we completely neglect the motion of matter, i.e., heating and cooling occur isochorically.

The model uses two-dimensional nonlinear two-temperature equations of thermal conductivity and exchange. In one-dimensional geometry, these equations were first proposed by S. I. Anisimov, B. L. Kapeliovich and T. L. Perelman, in a widely cited paper (Anisimov et al. 1974), which was written in 1974, long before the era of widespread use of femtosecond lasers. Two-dimensional equations are solved numerically using the alternating-direction implicit (ADI) technique developed by Peaceman and Rachford (1955) and Douglas (1955). The evolution of electron and ion temperatures in the case of a single light spot illuminated by a Gaussian beam is considered.

A two-dimensional two-temperature system of equations of a thermal model in plane geometry is written as:

$$\rho\frac{\partial e_e}{\partial t} = div(\kappa_e \, grad \, T_e) - \alpha_{ei}(T_e - T_i) + S(x, y, t), \tag{1}$$

$$\rho\frac{\partial e_i}{\partial t} = \alpha_{ei}(T_e - T_i). \tag{2}$$

Here e_e, e_i are the internal energies of the mass unit of electrons and ions, T_e and T_i are the electron and ion temperatures, and α_{ei} is the ion-electron coupling parameter that determines the rate of energy exchange between the electron and ion subsystems. The values of κ_e and α_{ei} are taken from (Petrov et al. 2015).

The model is closed by two-temperature equations of state (EOS) (Petrov et al. 2015; Khishchenko 1997, 2004, 2008, 2015, 2017; Levashov and Khishchenko 2007) for the electron and ion subsystems:

$$p_i = p_i(\rho, T_i),\ \ e_i = e_i(\rho, T_i),\ \ p_e = p_e(\rho, T_i, T_e),\ \ e_e = e_e(\rho, T_i, T_e). \tag{3}$$

Fermi-gas EOS is used for the electronic subsystem. The tabular semi-empirical multiphase EOS is used for the ion subsystem. Consideration of phase transitions makes the presented thermal model multi-phase. This allows for a more accurate accounting of the energy costs of melting, as opposed to approaches that consider the metal to be molten once it reaches the melting point. Such approaches ignore the melting process, in which the metal is not completely solid or completely liquid, but rather is in a separate volume in the form of a mixture of solid and melt. Also, they do not take into account the need for a very significant additional energy supply in order to completely melt the metal.

The energy source of the electronic subsystem (1) is as follows:

$$S(x, y, t) = \frac{F_{abs}}{\sqrt{\pi}\tau_L\delta}\left(exp\left(-\frac{x^2}{R_L^2}\right) - exp\frac{R_{box}^2}{R_L^2}\right)exp\left(-\frac{y}{\delta}\right)exp\left(-\frac{t^2}{\tau_L^2}\right). \tag{4}$$

The intensity distribution (4) corresponds to the radiation focused by a cylindrical lens. Radiation beam is directed from top to bottom, i.e. in the negative direction of the y-axis.

The maximum intensity is achieved at the point of the irradiated surface with the coordinate $x = 0$. This maximum corresponds to the value of the absorbed fluence

$$F = F_{abs}\left(1 - exp\left(-\frac{R_{box}^2}{R_L^2}\right)\right). \tag{5}$$

In the simulation we take $R_{box} = 500$ nm and $R_L = 180$ nm. Small correcting multiplier

$$exp\left(-\frac{R_{box}^2}{R_L^2}\right) = 4 \times 10^{-4} \tag{6}$$

is introduced to correct the intensity of the absorbed radiation so that at the edge points of the region $x = \pm R_{box}$. The intensity there is zero and there is no absorption.

2.3 Simulation and results

Thus, the computational domain is a box of $[-500, 500] \times [-50, 0]$ nm size. A uniform rectangular grid of 1000×50 cells was chosen for the simulation. The results are presented for the absorbed energy $F_{abs} = 500\,\mathrm{J/m^2}$. Simulation starts from the time moment $t = -5\tau_L$. By the time moment $t = 0$ a half of the laser pulse energy is absorbed.

The isothermal boundary condition $T_e = 300$ K (room temperature) is imposed on the right and left (side) boundaries of the film. Adiabatic boundary conditions

$$\frac{\partial T_e}{\partial y} = 0 \tag{7}$$

are imposed on the upper and lower boundaries (irradiated surface and back edge of the film).

Figures 2 and 3 show the evolution of the electron and ionic temperature fields. Note the difference between red colors on the figures: maximum T_e approximately equals about 13,000 K while maximum T_i hardly reaches the value of 3300 K. As indicated in the description in the previous section, for the first few picoseconds there is an alignment along the y axis, which is approximately the same time as the two-temperature stage. Then, in a few tens of picoseconds, the temperature is aligned along the x axis. Then, the metal cools and freezes.

Figure 4 shows the evolution of the melting zone obtained using the phase indicator tables from the EOS. Every pair of red and green bar denotes two zones: circular green zone inside the annular red zone. Green stripes cover the circle with fully molten metal. Red stripes indicate the annular fragments of the substance in which melting occurs, i.e. the metal is present as a mixture of solid and liquid phase. The region between red and green bar maximums is the mixing zone where the metal is present in both phases. Beyond the red bars area, the metal temperature is lower. Of course, simulation without special tracking of phase transitions and fronts of melting/crystallization does not allow to reflect quantitatively accurately the dynamics of the position of the zone boundaries at the late stages. But the qualitative result is quite acceptable, as evidenced by a good coincidence of the width of the melting zone at the time of 1 ns with the MD calculations presented in Inogamov et al. (2009).

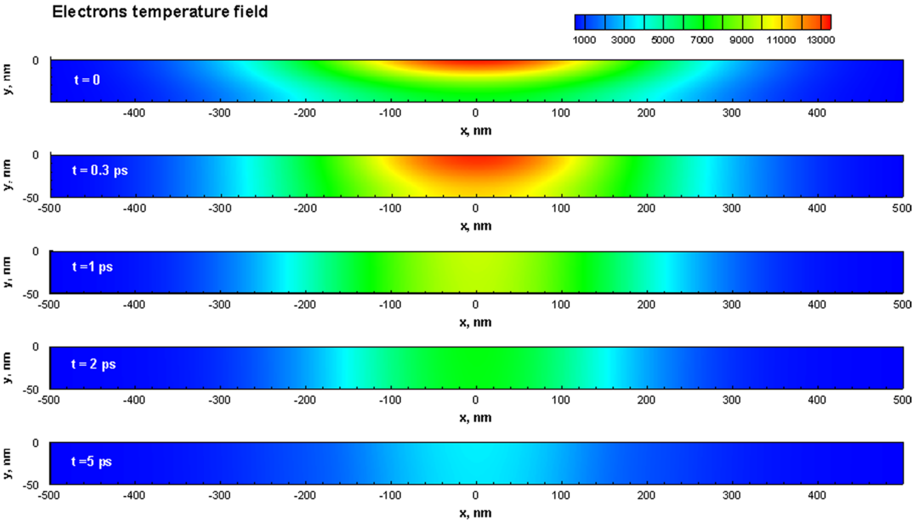

Fig. 2 T_e field at the time moments of 0, 0.3, 1, 2, 5 ps. Blue color corresponds the room temperature 300 K, red color corresponds to about 13,000 K. (Color figure online)

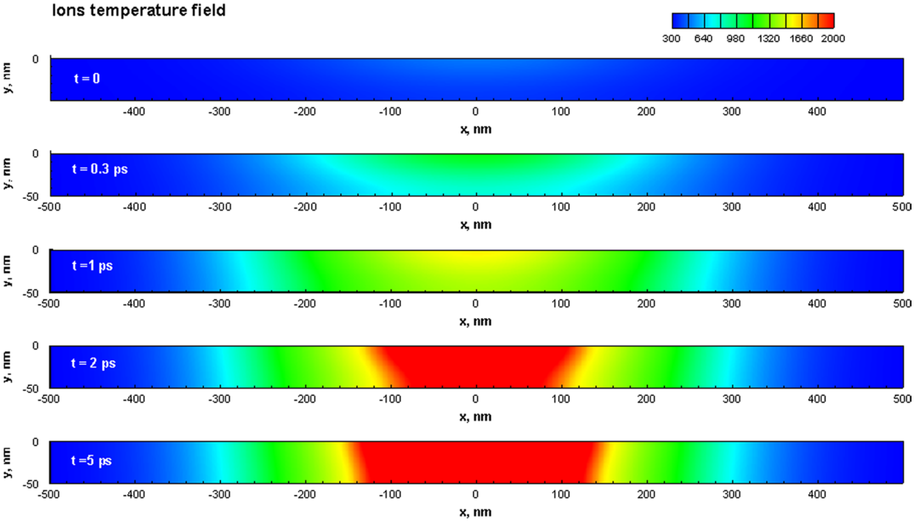

Fig. 3 T_e field at the time moments of 0, 0.3, 1, 2, 5 ps. Blue color corresponds the room temperature 300 K, red color corresponds to about 2200 K. (Color figure online)

2.4 Discussion

Let's discuss the the model presented.

Let's take a look to the phase diagram of aluminum on Fig. 5. Figure shows the curves of coexistence of solid, liquid and gas phases. Our model uses the wide-range equation of state.

Fig. 4 Radius of melting zone depending on time. Red bar marks the region containing the mix of solid and liquid phases of metal, while inside the green bar region the metal is fully molten. (Color figure online)

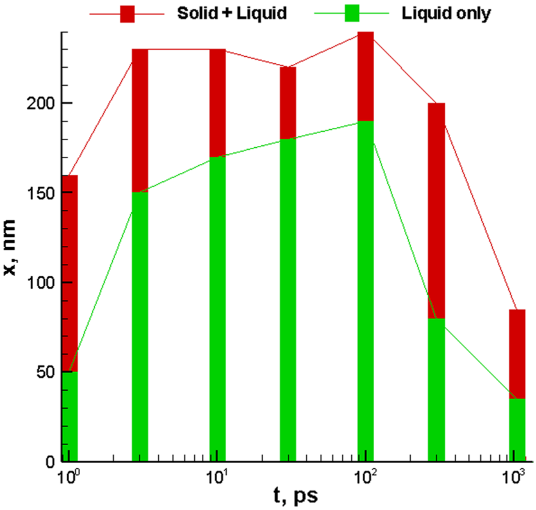

Fig. 5 The phase diagram of aluminum used in the heat model for the descrition of heat spreading inside the film. Tabular data was used according to Khishchenko (1997, 2004, 2008, 2015, 2017) and Levashov and Khishchenko (2007). The boundaries of phase transitions are shown: *c*-the condensation curve, *c.p.*-the critical point, *b*-the boiling curve, the black line segment—a triple point, *s*-the sublimation curve, *sol*-solidus, *liq*-liquidus, *i*-isochore density of 2.71 g/cm^3, which equals the density of aluminum at room temperature

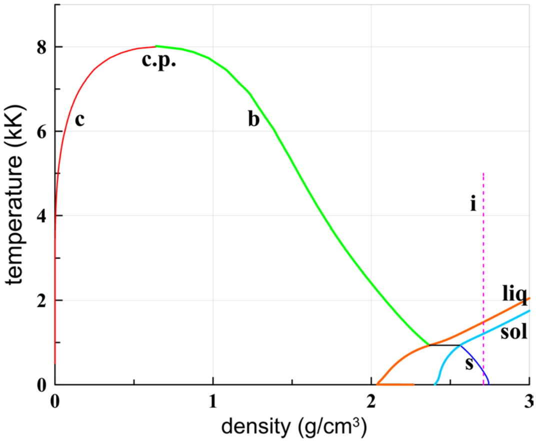

The advantage of the approach presented is taking into account the hidden heat of melting. The disadvantage is the approximation of the fixed substance. Therefore, the density of our film does not change with heating. This means that the distribution of ionic temperatures is always situated on the isochore of the initial density of aluminum. This is the isochore shown by the vertical dashed curve *i*on Fig. 5. The isochore begins on the sublimation curve at room temperature.

Our main task is to describe the initial stage of heating, which lasts from the beginning of heating the film with a femtosecond pulse and up to times of the order of the acoustic time scale $t_s = d_f / c_s$, where d_f is the thickness of the film, c_s is the speed of sound; the speed of sound varies moderately with the heats that interest us. For a film with a thickness of 50 nm and a sound speed of approximately 5 km/s, the duration of the acoustic stage is 10 ps. The main thing for us is to track the course of important events that occur at times that are less than the acoustic scale.

These events are as follows: the flow of absorbed laser energy from the skin layer of the order of 15 nm over the film thickness of 50 nm. In about a picosecond, as our model calculations show, the electronic temperature is aligned with the thickness of the film. Accordingly, the gradient of the electronic temperature at the coordinate y (this is the vertical to the film) decreases sharply. This gradient becomes of the order of the electron temperature gradient in the lateral direction x. Thus, it becomes essential to spread heat along the film from the heating spot to the periphery; cooling by transferring heat to the substrate at the specified time scales is neglected. This is true because the thermal conductivity of the glass substrate is small.

So, the first two important events are first the spreading of heat along the thickness along the coordinate y and then the spreading of heat along the film-the rotation of the heat flow from the direction y to the direction x. The third important event is related to the temperature equalization of the electron and ion subsystems. It occurs on a time scale of 2–5 ps. Why is this event important?

The fact is that after the temperature equalization, the coefficient of electronic thermal conductivity decreases sharply. Accordingly, the propagation of heat to the sides of the heating spot on the film is sharply inhibited. In our calculations, we use a model of the thermal conductivity of aluminum, which continuously describes through both two-temperature and one-temperature states together with a jump in the thermal conductivity coefficient during melting (Inogamov and Petrov 2010). Note that the propagation deceleration occurs before the end of the isochoric stage; the duration of the isochoric stage is determined by the acoustic time scale t_s. At the isochoric stage, it is permissible to use an approximation that does not take into account the processes of thermal expansion of the substance. Section 3 is devoted to accounting for this extension.

Therefore, spot heating, which is to top acoustic stage is determined by how greatly expand spot heating in comparison with the laser spot radius R_L. Our calculations show that the broadening of the spots compared with R_L is in the case of aluminium approximately $d_T \sim$ of 100–150 nm. Thus, instead of spot with radius R_L we get a spot with radius $R_L + d_T$. See that the effect of thermal broadening is important only for very small values of R_L. Small values of the radius of the beam are obtained by focusing at the diffraction limit (when $R_L \sim \lambda$) and when using ultraviolet radiation $\lambda \sim 200{-}300$ nm; λ -wavelength of the applied radiation.

Why is the size of the heating spot formed at the beginning of the acoustic stage so important for describing the laser impact on the film? The fact is that the accumulation of the reactive impulse by the film due to the mechanical recoil from the substrate continues for a period of time on the order of the acoustic time scale (Inogamov and Zhakhovskii 2014). If the film has accumulated sufficient momentum in the direction of the vacuum, it breaks away from the substrate. If not, it remains on the substrate. Momentum accumalated is equal to $\rho\, d_F\, v = \int_{-\infty}^{t_{sep}} p\, dt$ at a given point of the film is determined by the pressure $p(t)$ at the film-substrate boundary; here t_{sep} the time at which the film is separated from the substrate, $t_{sep} \sim t_s$. In turn, this pressure depends on the history of heating—that is, the history of temperature increase at this point of the film. It is clear that the heats outside the heating spot are small. Therefore, the film points outside the heating spot in Fig. 2 will not be able to break away from the substrate.

Determining the effective spot radius $R_L + d_T$ is crucial for applying the Liu (1982) approach. In this approach, it is assumed that the intensity distribution, and hence the fluence over the heating spot, is described by the Gauss function. Further, it is believed that the reflection coefficient does not depend on the intensity—that is, it is uniform in the heating spot. Then the absorbed energy (absorbed fluence) is also given by the

Gauss function. Our problems of heat propagation, of course, operate with the absorbed fluence F.

Let $F = F_c \exp(-x^2/R_L^2)$, F_c being the fluence value in the center of the spot. Let F_a be the threshold fluence: above this fluence, the film breaks away from the substrate, below this, the cohesion forces between the film and the substrate hold the film on the substrate. Let x_a be the radius of the separation spot; we use the same terms (radius) for the cases of cylindrical lighting and axisymmetric lighting. Then logarithmizing the equality $F_a = F_c \exp(-x_a^2/R_L^2)$, we get an important dependence

$$x_a^2 = R_L^2 \ln(F_c/F_a).$$

This dependence is most widely applied by experimenters. Fix the size of the beam (fix the focusing optics) and vary the pulse energy. As a result, the parameter F_c changes proportionally. This allows you to determine two important parameters: the ablation threshold F_a and the beam radius R_L.

The radius determined by the method of Liu (1982) is equal to the radius of the laser beam only in the case when there is no spreading of heat from the light spot. That is, no broadening of the heating spot up to the time of separation film inside the region $|x| < x_a$. If there is widening, and it takes place before the moment of separation, it will be determined not by the radius of the spot light, and the radius of the heating spot $R_L + d_T$, i.e. the effective radius.

As you can see, the separation or non-separation of the film from the substrate is determined solely by the heating history of the local point. Below (Sect. 3) we will analyze a fundamentally different mechanism of separation associated with the propagation of a shock wave in the substrate under the film.

It is clear that the Liu technique can work in the case when the vertical size, i.e. the coordinate y, heating area is much (several orders of magnitude) smaller than the vertical size. The technique with the real radius of the laser beam R_L (not $R_L + d_T$) is applicable when the effects are strictly local, and at each point are determined by the absorbed energy at that point. In this case, the result at this point does not depend on what energy is absorbed at neighboring points.

This paper reports on two mechanisms of violation of the Liu methodology. First, it is a rapid (at times smaller than the acoustic scale) removal of heat by electronic thermal conductivity beyond the radius R_L of the lighting spot. This possibility is due to the supersonic rate of heat propagation through the electronic subsystem at the stage with two-temperature States of matter. Second, it is a hydrodynamic mechanism associated with a shock wave in the substrate (Sect. 3). Of course, both mechanisms arise in connection with deviations from locality—because of the influence of side sections (in relation to a given point of the film) on what is happening at a given point.

Let us now discuss what happens at distant times that exceed the acoustic time scale t_s at these times, the displacements of matter are significant, the constant density approximation (isochoric approximation) is only suitable in order of magnitude. So, at small times $t < t_s$ the density changes are small, the main part of the substance is located on the isochore i in Fig. 5. At large times, it is reasonable to replace the isochoric approximation with the Isobaric approximation. In this case, the substance on the phase plane is located along the sections s and b of the binodal (phase coexistence curve) on Fig. 5.

At the early isochoric stage, at our temperatures, there is a significant area of solid-liquid phase mixture. This mixture corresponds to the segment of the isochore i between the solidus *sol* and the liquidus *liq* on Fig. 5. In this case, the approximation of the Stefan problem is not applicable to describe the propagation of melting on the film. At the isobaric stage, the situation is the opposite. The mixture disappears, forming a sharp melting front that separates the pure solid and liquid phases. The melting zone expands to the maximum. Then the recrystallization stage begins. Our model with an isochore approximately (in order of magnitude) describes what happens at long times $t > t_s$, describes the propagation of melting and subsequent recrystallization.

Note that the separation of the film from the substrate does not interfere with the flow of heat along the film. Of course, due to the lengthening and thinning of the film, the heat transfer changes, but in quality terms, the situation remains the same. This is due to the fact that the main heat transfer occurs along the film—the heat transfer to the substrate is small.

The model used allows us to estimate the thermal contribution to the expansion of the heating region in the first few tens of picoseconds. This is important because the width of the heating area determines the size of the delamination zone of the film from the substrate. This size in turn affects the size of the resulting surface structures.

Also, with the help of the model, we can estimate the space-time scales of heating and cooling of the light spot. We see that the maximum width of the melting zone is reached at a time of about 100 ps. But at the time when delamination begins (20–30 ps) the width is not too much higher than the spot area. And before full recrystallization of the film with $F_{abs} = 500\,\text{J/m}^2$ and $R_L = 180$ nm, a time interval of about 1.2 ns is required. The solidification stage is important because during this stage the macroscopic movement of the surface structures formed during ablation stops and their shape is preserved for further analysis.

3 Dynamic model

Numerous existing works and approaches take into consideration only the state of the film itself. It is advisable to exclude the substrate from consideration in numerical simulations, because it saves computational resources. Experimental studies usually do not have the means to monitor the substrate, paying all attention to the observation of the film. Further, however, we will show that at certain values of the absorbed fluences, spatial effects in the substrate have a strong influence on the resulting nanostructures, up to a significant change in their shape.

3.1 Overall description of the effect

Consider the problem of single-pulse subpicosecond ablation of a thin gold film deposited on a substrate of laboratory glass. In a similar setting, a series of full-scale experiments (Wang et al. 2017) with the 50 nm-thick golden film deposited on 100 μm-thick silica glass substrate. Second harmonic was used with wavelength $\lambda = 515$ nm, duration of the pulse was $\tau_L = 200$ fs and numerical aperture was $NA = 0.25$. At sufficiently large absorbed fluences as a result of ultrashort laser irradiation holes began to form. The size of the holes grew with increasing intensity of radiation, and could exceed the size of the light spot several times, see Fig. 6.

The reasons for this phenomenon become clear if we include in the consideration of the hydrodynamic motion of the substrate. Figure 7 shows the general scheme of the mechanism.

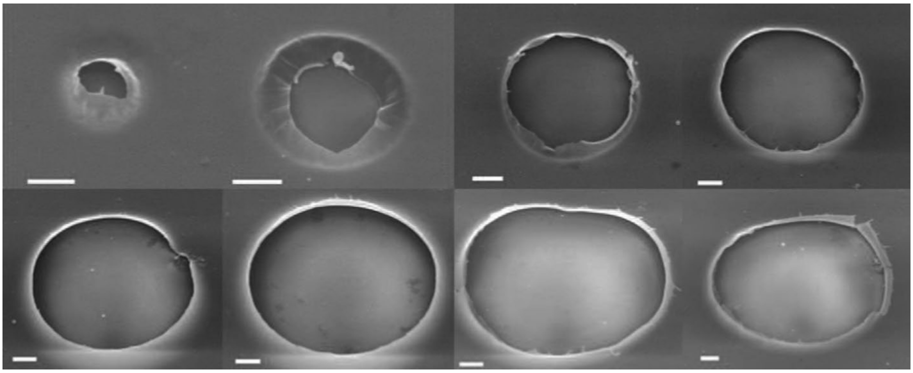

Fig. 6 The photos of the holes (Wang et al. 2017) obtained by scanning electron microscope (SEM) technique

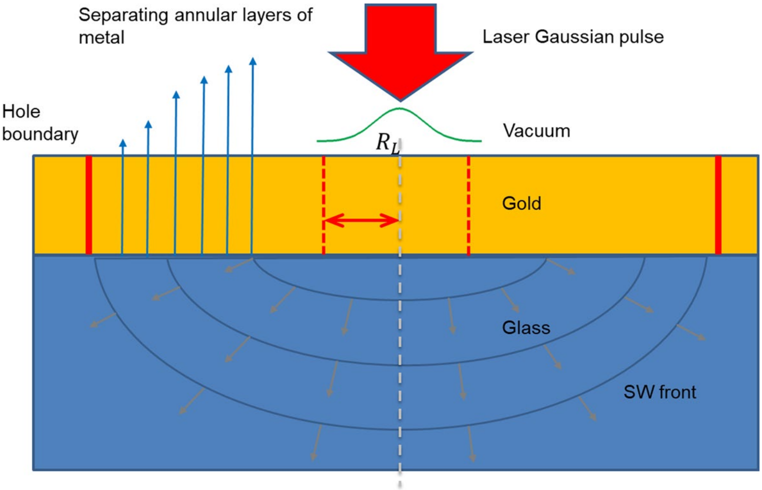

Fig. 7 Holes formation effect scheme due to the shockwave in the glass substrate

For the first few picoseconds, the area of the light spot in the film has time to warm up strongly in the longitudinal direction, from the front wall to the border with the substrate. The boundary of the film with the substrate then becomes the source of the compression wave in the substrate. This effect lasts for a limited time until the high pressure area in the film disintegrates. Initially, a plane compression wave propagates in the substrate in the longitudinal direction, deep into the substrate. Then the wave front gradually spherizes, the compression profile tilts and becomes triangular due to the rarefaction wave catching up with it. As a result, already at a distance approximately equal to R_L, the perturbation is a triangular spherical shock wave. The magnitude of the jump at the front of the wave decreases rapidly as it propagates. This effect is essentially two-dimensional (taking into account the axial symmetry) and can not be obtained using a one-dimensional hydrodynamic code. After passing the distance R_L, the wave continues to spread in the glass and fade. Its front is an expanding hemisphere, which also passes through the boundary between the film and the substrate. As the wave passes through the boundary, the boundary points accumulate momentum directed from the substrate in the film. When this momentum becomes sufficient, delamination of the film from the substrate occurs at the place where the magnitude of the impulse is large enough. Due to the axial symmetry of the wave, we can talk about the gradual delamination of the ring layers of the film from the substrate. The accumulated momentum decreases as the distance from the center of the light spot, and at some point it becomes insufficient for separation. At this point, delamination stops. Thus, this process can be described as a shock-wave mechanism of hole formation under ultrashort laser irradiation of a thin film. The thermal mechanism does not allow to explain this effect as it excludes essential influence of laser heating outside of a light spot.

3.2 Model equations

The proposed one-temperature model and algorithm are based on Euler equations of motion of a compressible ideal medium in plane two-dimensional geometry. In conservative form they can be written as

$$\frac{\partial \rho}{\partial t} + \frac{\partial(\rho u)}{\partial x} + \frac{\partial(\rho v)}{\partial y} = 0, \tag{8}$$

$$\frac{\partial \rho u}{\partial t} + \frac{\partial(p + \rho u^2)}{\partial x} + \frac{\partial(\rho u v)}{\partial y} = 0, \tag{9}$$

$$\frac{\partial \rho v}{\partial t} + \frac{\partial(\rho u v)}{\partial x} + \frac{\partial(p + \rho v^2)}{\partial y} = 0, \tag{10}$$

$$\frac{\partial \rho E}{\partial t} + \frac{\partial(u(p + \rho E))}{\partial x} + \frac{\partial(v(p + \rho E))}{\partial y} = 0. \tag{11}$$

where ρ is the density, u, v is the x- and y-components of velocity, p is the pressure, e is the internal, and $E = e + 1/2u^2 + 1/2v^2$ is the total energy of the mass unit. The equations of the model are closed by the equation of state

$$p = p(\rho, e). \tag{12}$$

The model is needed primarily to detect the effect and describe the stages of the process. It is not required to accurately display the shape and size of the resulting nanostructures. Therefore, we will be satisfied, with some reservations, with the EOS of the ideal gas $p = (\gamma - 1)\rho e$, $\gamma = 3$. We will not describe in detail the process of radiation absorption characteristic of the 2T-stage of ultrashort ablation, rapid energy transfer deep into the film due to electronic thermal conductivity and further heating and temperature equalization in the film due to electron-ion relaxation. These processes are described in detail in the works (Inogamov and Zhakhovskii 2014; Inogamov et al. 2015, 2016a, b; Inogamov and Zhakhovsky 2016) and we well represent the shape of the resulting compression profile in the film. Therefore, we will limit ourselves to the task of the Gaussian initial pressure perturbation, which describes with sufficient accuracy the result of real heating of the film at the 2T-stage. The ionic thermal conductivity in our conditions is also negligible.

3.3 Gas dynamic approach

To be sure, an ideal gas is a pretty rough approximation to describe a condensed medium. However, from the point of view of the principle of rationality of numerical modeling, its use is quite justified, since this approximation is sufficient for fixing and step-by-step description of the effect. It is required to present a plausible physical picture, close to the real picture of the condensed matter flow. This is achieved in the present model in two ways. First, we choose the initial conditions so that the wave pattern is as close to reality as possible. Namely, we strive for such a ratio of pressures and densities that the sound velocity of the resulting medium in the metal region was close to its bulk modulus.

Secondly, we introduce a background pressure of $p_{ini} = 100$ GPa, $1\,\mathrm{GPa} = 10^9$ Pa, which is conventionally considered zero. It is supported by gas in a vacuum. That is, we replace the vacuum with a low-density hot gas with a background pressure of 100 GPa. Dynamically, in two-dimensional motion, the presence of such a gas is insignificant because of its low density. Further in the calculations we will monitor the pressure adjusted for the background i.e. for the value $p - p_{ini}$. Thus, we ensure that the pressure is equal to zero under normal conditions and that the contact boundaries are fixed in the non-heated areas. At the same time, the background pressure allows us to approximate the situation with a condensed medium in which, when expanding beyond the equilibrium specific volume, a negative pressure appears. Here, if we encounter a pressure below p_{ini} in the simulation, we will understand that we are observing a region where the substance is stretched by the substance.

It turns out that we use in the model a simple and universal description of the properties of a substance, which in different ranges of values of variables exhibits different properties. The description of the glass is also satisfactory, since the sound velocities in gold and glass are in order the same as the real ones. And in the area of small densities in the air or vacuum zone, the environment behaves as ideal, which is what we need. At the same time, a single EOS for all three substances allows not to use multiphase/multi-liquid models for the correct description of the flow in the areas of contact discontinuities.

3.4 Simulation and results

The simulation is performed using a hydrodynamic code that implements Godunov-type finite-volume method on a uniform rectangular grid. To calculate the intercell fluxes, we use a Riemann solver based on the exact solution of the problem of the desintegration of an arbitrary discontinuity. The first implementation of the numerical algorithm used a first-order accuracy method in time and space. Here we improved the algorithm by increasing the order over the space up to the second one using slope limiter. Slope limiters are used in high resolution schemes, to avoid the spurious oscillations (wiggles) that would otherwise occur with high order spatial discretization schemes due to shocks, discontinuities or sharp changes in the solution domain. Use of flux limiters, make the solutions satisfy total variation diminishing (TVD) property. Simple *minmod* slope limiter is used in our implementation of the computational algorythm.

The second-order method allows to obtain a fairly accurate resolution of discontinuities of gas-dynamic variables, whereas the first-order methods strongly smudge them. The spatial approximation used in the method is unsplit, and the method is quite stable at Courant–Friedrichs–Lewy (CFL) parameter values from the range of 0.3–0.4.

The computational domain is divided into three layers with a single EOS of matter and different initial conditions: glass, metal, and vacuum. The film thickness is 50 nm, the glass and vacuum thicknesses are 1200 nm and 1000 nm respectively. The density of glass equals 2300 kg/m^3, the density of gold equals 19,300 kg/m^3, and the density of vacuum 200 kg/m^3. The background pressure in all three areas is 100 GPa, which ensures the stability of the contact boundary over time in the non-heated area. The initial pressure disturbance of the Gaussian form is imposed on the metal layer:

$$p_{dist}(x) = p_{ini} + (p_{heat} - p_{ini}) exp\left(-\frac{x^2}{R_L^2} \right). \tag{13}$$

We model the experiment from Wang et al. (2017) with absorbed fluence $F_{abs} = 4000\,\mathrm{J/m^2}$. The pressure at the maximum of initial heated Gaussian profile is $p_{heat} = 1000$ GPa. For reasons of symmetry it is enough to take to include only the right half of the target to the simulation box, which is the rectangle $[0, 1200] \times [-1200, 1050]$ (nm). Symmetric boundary conditions thus are imposed on the left boundary, and transmissive boundary conditions are imposed on the other three boundaries, so as not to impede the passage of any perturbations. Uniform rectangular grid of 240×450 cells was chosen for the simulation.

The simulation shows us in detail the stages of the process described above. In the first few picoseconds, plane wave propagation takes place, see pressure $p - p_{ini}$ fields on Figs. 8 and 9. Figures 10, 11 and 12 show the gradual spherization and by the time moment $t = 60$ ps we observe a fully formed hemispherical front. Figs. 13, 14, 15, 16 and 17 show corresponding density field diagrams.

Now we introduce a criterion description of the film separation from the substrate into the model. To do this, consider an arbitrary layer of cells adjacent to the boundary and evaluate its ability as a result of the passage of the shock wave to accumulate sufficient momentum for delamination of the adjacent metal layer. For observation we choose N

Fig. 8 Pressure $p - p_{ini}$ field at the moment $t = 0$ ps

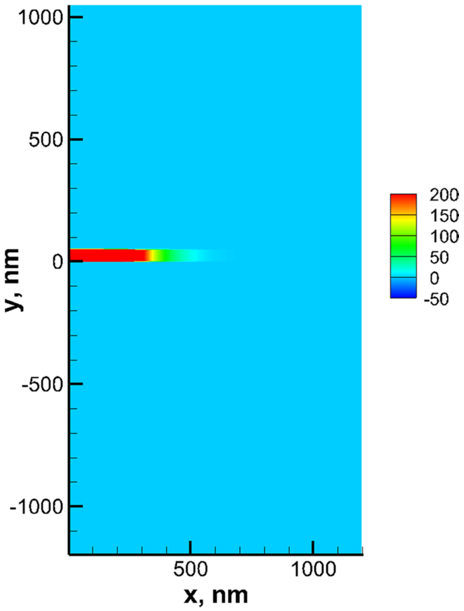

Fig. 9 Pressure $p - p_{ini}$ field at the moment $t = 10$ ps

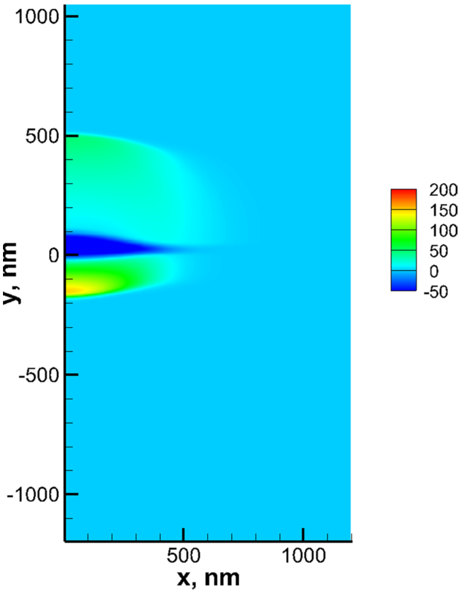

Fig. 10 Pressure $p - p_{ini}$ field at the moment $t = 20$ ps

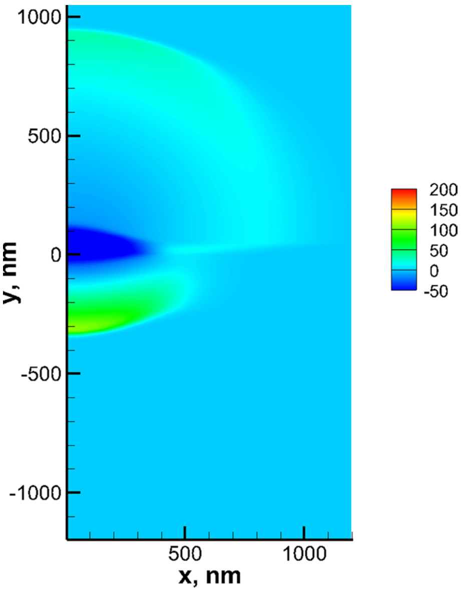

control points lying on the line $y = -40$ nm. It is enough to take N equal to 11 for 10 equal distances, because the central point and the boundary point also included, see Fig. 11. By writing down Newton's second law for the resulting layers, we can estimate the momentum of each layer. For the case of a gold film on the glass, adhesion is practically absent, i.e. we can assume that the ejection impulse of the glass layer will be determined only by the

Fig. 11 Pressure $p - p_{ini}$ field at the moment $t = 40$ ps. 10 tracking points are set along $y = -40$ nm line to monitor accumulating momentum

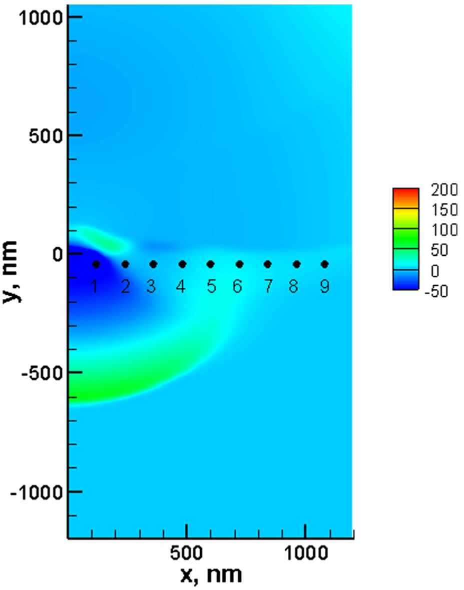

Fig. 12 Pressure $p - p_{ini}$ field at the moment $t = 60$ ps

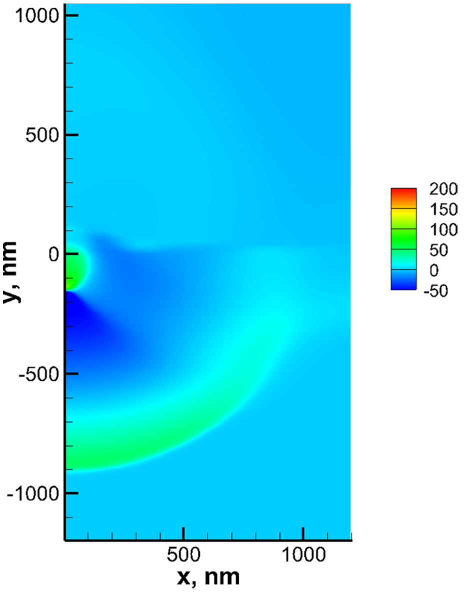

difference in hydrodynamic pressures at the ends of this layer. Writing down Newton's second law for i-th tracking layer in the following form:

$$\rho_0 d_F v_i(t) = \int_0^{+\infty} (p_i(\tau) - p_{ini})\, d\tau, \tag{14}$$

Fig. 13 Density field at the moment $t = 0$ ps

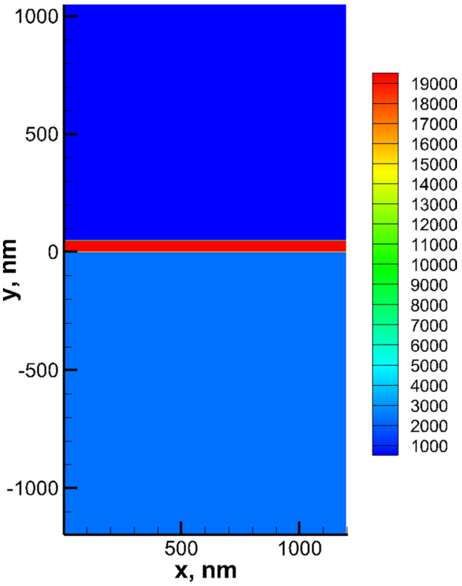

Fig. 14 Density field at the moment $t = 10$ ps

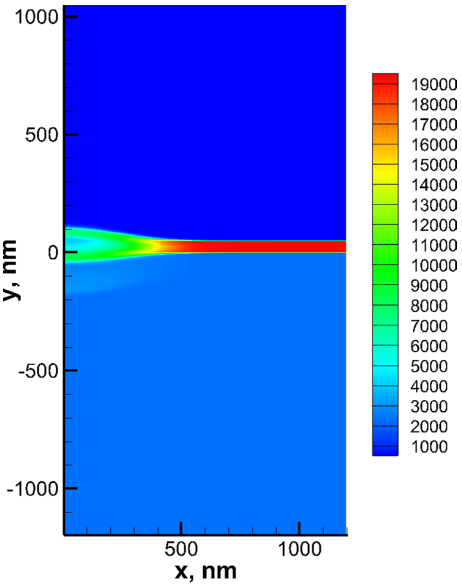

and expressing from it the temporal dependence of velocity, we obtain

$$v_i(t) = \frac{\int_0^{+\infty} (p_i(\tau) - p_{ini})\, d\tau}{\rho_0 d_F}. \tag{15}$$

Fig. 15 Density field at the moment $t = 20$ ps

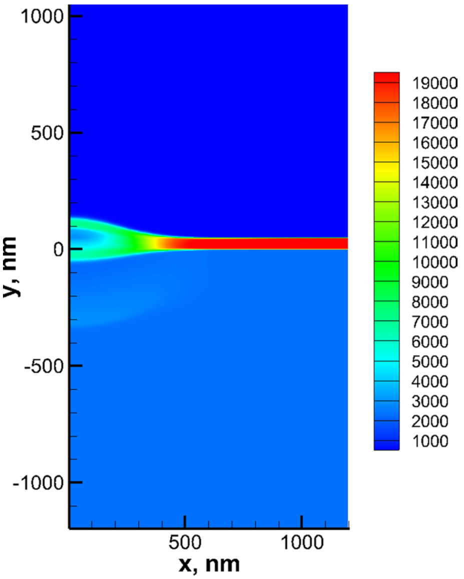

Fig. 16 Density field at the moment $t = 40$ ps

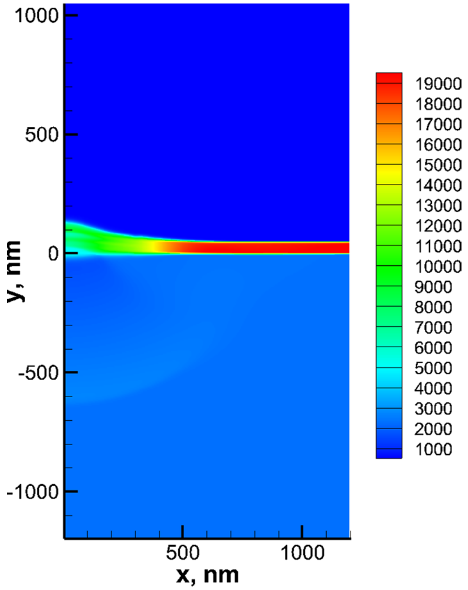

$\rho_i(t)$ is the temporal dependency of the average density of the i-th tracking layer and $p_i(t)$ is the pressure from the disturbed medium to the tracking layer. $d_F = 50$ nm is the thickness of the gold layer.

Thus, numerically integrating the dependence of the pressure at the control points on the time during the simulation, we obtain the values of the velocity "accumulated" by the substrate layer relating to the selected control point. From one-dimensional calculations, we know the value of the rate that is needed for delamination to occur (Wang et al. 2017).

Fig. 17 Density field at the moment $t = 60$ ps

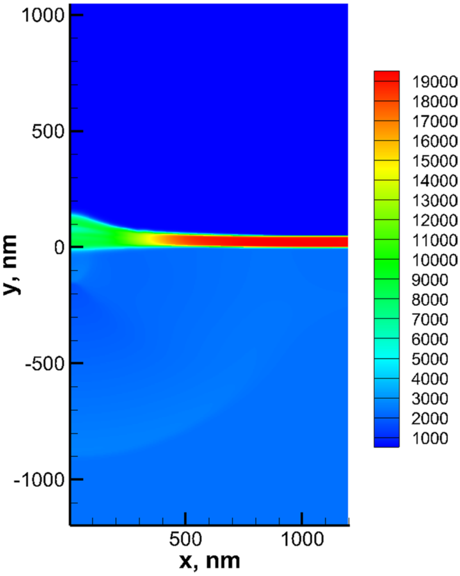

This value is about 30 m/s. Thus, for the resulting 10 boundary points, we will know the dependence of the accumulated velocity on time, and we will be able to apply the separation criterion: the separation occurs only when the value $v_i(t)$ reaches the required threshold value.

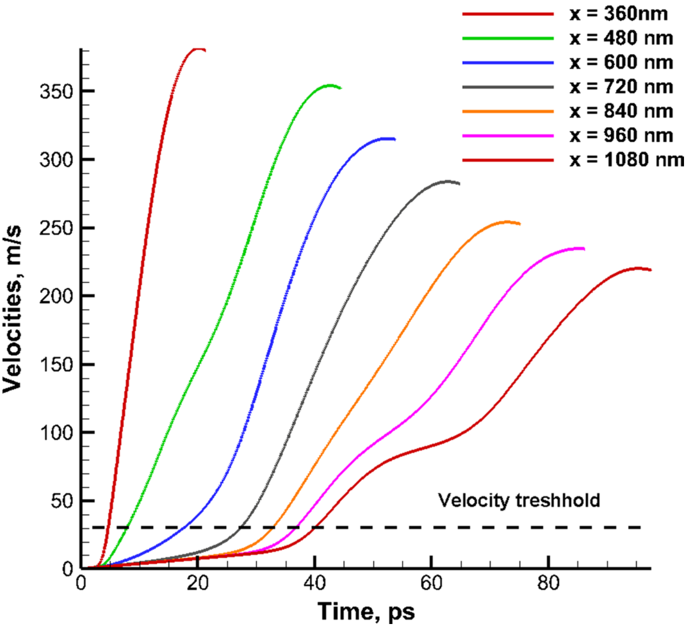

Fig. 18 Velocities evolution of the tracking points. The threshold equals 30 m/s

Figure 18 shows the velocity versus time relationships at the selected tracking points. We doesn't include three points inside the focal spot region with $x = 0, 120$ nm and 240 nm, their velocities, as expected, are growing too fast. It is easy to see that separation will occur at all control points, and we need to extrapolate the available dependencies to determine the x-coordinate of the point at which the maximum velocity does not exceed the threshold value. This will be the radius of the hole. Linear extrapolation gives a radius value of about 4 μm. In the full-scale experiment with the absorbed fluence of 4000 J/m^2, the radius of the hole is about 5 μm. Such an agreement is certainly pleasant, but largely accidental. The model, however, makes it possible to obtain an accurate qualitative and physically consistent description of the effect.

In the future, the computational algorithm can be improved, first of all, by introducing real, rather than model EOS. It can be either more simple EOS like Mie-Gruneisen, or more complex tabular multi-phase wide-range dependence. Also, the physical accuracy of the descriptions can be improved by adding a multi-fluid model and kinetic corrections for taking accurately into account breaks in the metal or at the metal-glass interface.

3.5 Summary

Two complementary two-dimensional models are presented to describe the thermal and dynamic effects of single-pulse ultrashort laser ablation of thin films on glass substrates. The thermal model describes the 2T-stage of laser heating of the film, the subsequent lateral energy transfer in the metal, cooling and recrystallization. The dynamic model presents the effect of hole formation in the film due to the shock-wave mechanism, the main driver of which is the two-dimensional hydrodynamic effects in the substrate.

Acknowledgements Authors (VVS, SVF) were supported by the State assigment for Institute for Computer Aided Design of the Russian Academy of Sciences (RAS). Author (NAI) was supported by the State assigment for L.D. Landau Institute for Theoretical Physics of the RAS (no. 0033-2019-0007).

References

Anisimov, S.I., Kapeliovich, B.L., Perelman, T.L.: Electron emission from metal surfaces exposed to ultrashort laser pulses. Sov. Phys. JETP **39**(2), 375–377 (1974)

Bonse, J., Höhm, S., Kirner, S.V., Rosenfeld, A., Krüger, J.: Laser-induced periodic surface structures: a scientific evergreen. IEEE. J. Sel. Top. Quantum Electron. **23**(3), 9000615 (2017)

Douglas, Jim: On the numerical integration of parabolic equation by implicit methods. J. Soc. Ind. Appl. Math. **3**(1), 42–65 (1955)

Fang, R., Vorobyev, A., Guo, C.: Direct visualization of the complete evolution of femtosecond laser-induced surface structural dynamics of metals. Light Sci. Appl. **6**, e16256 (2017)

Inogamov, N.A., Petrov, Yu.V.: Thermal conductivity of metals with hot electrons. J. Exp. Theor. Phys. **110**(3), 446–468 (2010)

Inogamov, N.A., Zhakhovskii, V.V.: Formation of nanojets and nanodroplets by an ultrashort laser pulse at focusing in the diffraction limit. JETP Lett. **100**(1), 4–10 (2014)

Inogamov, N.A., Zhakhovsky, V.V.: Surface 3D nanostructuring by tightly focused laser pulse: simulations by Lagrangian code and molecular dynamics. J. Phys. Conf. Ser. **681**, 012001 (2016)

Inogamov, N.A., Zhakhovskii, V.V., Ashitkov, S.I., Khokhlov, V.A., Petrov, Yu.V., Komarov, P.S., Agranat, M.B., Anisimov, S.I., Nishihara, K.: Two-temperature relaxation and melting after absorption of femtosecond laser pulse. Appl. Surf. Sci. **255**(24), 9712–9716 (2009)

Inogamov, N.A., Ashitkov, S.I., Zhakhovsky, V.V., Shepelev, V.V., Khokhlov, V.A., Komarov, P.S., Agranat, M.B., Anisimov, S.I., Fortov, V.E.: Acoustic probing of two-temperature relaxation initiated by action of ultrashort laser pulse. Appl. Phys. A **101**(1), 1–5 (2010)

Inogamov, N.A., Zhakhovskii, V.V., Khokhlov, V.A., Shepelev, V.V.: Superelasticity and the propagation of shock waves in crystals. JETP Lett. **93**(4), 226–232 (2011)

Inogamov, N.A., Zhakhovskii, V.V., Khokhlov, V.A.: Jet formation in spallation of metal film from substrate under action of femtosecond laser pulse. JETP **120**(1), 15–48 (2015)

Inogamov, N.A., Zhakhovsky, V.V., Khokhlov, V.A., Petrov, Yu.V., Migdal, K.P.: Solitary nanostructures produced by ultrashort laser pulse. Nanoscale Res. Lett. **11**(1), 177 (2016a)

Inogamov, N.A., Zhakhovsky, V.V., Migdal, K.P.: Laser-induced spalling of thin metal film from silica substrate followed by inflation of microbump. Appl. Phys. A **122**(4), 432 (2016b)

Khishchenko, K.V.: Temperature and heat capacity of polymethyl methacrylate behind the front of strong shock waves. High Temp. **35**(6), 991–994 (1997)

Khishchenko, K.V.: The equation of state for magnesium at high pressures. Tech. Phys. Lett. **30**(19), 829–831 (2004)

Khishchenko, K.V.: Equations of state for two alkali metals at high temperatures. J. Phys. Conf. Ser. **98**(3), 032023 (2008)

Khishchenko, K.V.: Equation of state for tungsten over a wide range of densities and internal energies. J. Phys. Conf. Ser. **653**, 012081 (2015)

Khishchenko, K.V.: Equation of state of sodium for modeling of shock-wave processes at high pressures. Math. Montisnigri **40**, 140–147 (2017)

Kryukov, P.G.: Femtosecond Pulses: Introduction to New Field of Laser Physics. Fizmatlit, Moscow (2008). (**in Russian**)

Levashov, P.R., Khishchenko, K.V.: Tabular multiphase equations of state for metals and their applications. AIP Conf. Proc. **955**, 59–62 (2007)

Liu, J.M.: Simple technique for measurements of pulsed Gaussian-beam spot sizes. Opt. Lett. **7**(5), 196–198 (1982)

Meshcheryakov, Y., Bulgakova, N.: Thermoelastic modeling of microbump and nanojet formation on nanosize gold films under femtosecond laser irradiation. Appl. Phys. A: Mater. Sci. Process. **82**, 363 (2006)

Meshcheryakov, Y.P., Shugaev, M.V., Mattle, T., Lippert, T., Bulgakova, N.M.: Role of thermal stresses on pulsed laser irradiation of thin films under conditions of microbump formation and nonvaporization forward transfer. Appl. Phys. A: Mater. Sci. Process. **113**, 521–529 (2013)

Nakata, Y., Okada, T., Maeda, M.: Generated, nano-sized hollow bump array, by single femtosecond laser pulse. Jpn. J. Appl. Phys. **42**(2), 12A (2003)

Peaceman, D.W., Rachford, H.H.: The numerical solution of parabolic and elliptic differential equations. J. Soc. Ind. Appl. Math. **3**(1), 28–42 (1955)

Petrov, Yu.V., Migdal, K.P., Inogamov, N.A., Zhakhovsky, V.V.: Two-temperature equation of state for aluminum and gold with electrons excited by an ultrashort laser pulse. Appl. Phys. B **119**(3), 401–411 (2015)

Vorobyev, A.Y., Guo, C.: Femtosecond laser nanostructuring of metals. Opt. Express **14**, 2164–2169 (2006)

Wang, X.W., Kuchmizhak, A.A., Li, X., Juodkazis, S., Vitrik, O.B., Kulchin, Yu.N., Zhakhovsky, V.V., Danilov, P.A., Ionin, A.A., Kudryashov, S.I., Rudenko, A.A., Inogamov, N.A.: Laser-induced translative hydrodynamic mass snapshots: noninvasive characterization and predictive modeling via mapping at nanoscale. Phys. Rev. Appl. **8**, 044016 (2017)

Affiliations

V. V. Shepelev[1] · N. A. Inogamov[2] · S. V. Fortova[1]

[1] Institute for Computer-Aided Design, Russian Academy of Sciences, Vtoraya Brestskaya St., 19/18, Moscow, Russia 123056

[2] Landau Institute for Theoretical Physics, Russian Academy of Scienses, Akademika Semenova St., 1a, Chernogolovka, Moscow Region, Russia 142432